Photoacoustics 28 (2022) 100409

Contents lists available at ScienceDirect

Photoacoustics

journal homepage: www.elsevier.com/locate/pacs

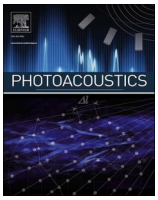

Photoacoustic imaging for the study of oxygen saturation and total hemoglobin in bone healing and non-union formation

Maximilian M. Menger [a,b,*], Christina Körbel [b], David Bauer [b], Michelle Bleimehl [b], Anne L. Tobias [b], Benedikt J. Braun [a], Steven C. Herath [a], Mika F. Rollmann [a], Matthias W. Laschke [b], Michael D. Menger [b], Tina Histing [a]

[a] Department of Trauma and Reconstructive Surgery, Eberhard Karls University Tübingen, BG Trauma Center Tübingen, 72076 Tübingen, Germany
[b] Institute for Clinical & Experimental Surgery, Saarland University, 66421 Homburg, Saar, Germany

ARTICLE INFO

Keywords:
Photoacoustic imaging
Oxygen saturation
Vascularization
Angiogenesis
Microvessel density
Non-union
Bone healing
Mice

ABSTRACT

Non-union formation represents a major complication in trauma surgery. Adequate vascularization has been recognized as vital for bone healing. However, the role of vascularization in the pathophysiology of non-union formation remains elusive. This is due to difficulties in studying bone microcirculation in vivo. Therefore, we herein studied in a murine osteotomy model whether photoacoustic imaging may be used to analyze vascularization in bone healing and non-union formation. We found that oxygen saturation within the callus tissue is significantly lower in non-unions compared to unions and further declines over time. Moreover, the amount of total hemoglobin (HbT) within the callus tissue was markedly reduced in non-unions. Correlation analyses showed a strong positive correlation between microvessel density and HbT, indicating that photoacoustically determined HbT is a valid parameter to assess vascularization during bone healing. In summary, photoacoustic imaging is a promising approach to study vascular function and tissue oxygenation in bone regeneration.

1. Introduction

Fracture healing is a complex and highly orchestrated process that has been extensively studied in humans and a variety of animal models. Despite increasing insights into the molecular and cellular basis of bone healing, 10% of all fractures still result in delayed healing or non-union formation [1]. Delayed unions and, in particular, non-unions do not only result in chronic pain, loss of function and prolonged rehabilitation for the patient, but also impose a considerable economic burden to society [2]. Notably, in a substantial amount of cases the reason for non-union formation remains largely unclear and, thus, effective prevention and treatment strategies are lacking.

Vascularization has been recognized as crucial for successful bone healing [3]. In fact, newly formed microvessels allow mesenchymal stem cells to invade the fracture site, resulting in callus formation and remodeling from avascular cartilage towards mineralized woven bone [4]. However, the role of vascularization and the functionality of the microvasculature in non-unions are controversially discussed throughout the literature. Several studies consider non-unions as the result of an avascular and biologically inert environment [5,6]. On the other hand, various histological studies demonstrated that the callus tissue of established non-unions is indeed considerably vascularized [7–9]. Accordingly, further research is required to fully understand the role of vascularization in the pathophysiology of non-union formation.

Photoacoustic imaging is a novel imaging technique that uses thermoelastic expansion of tissues to generate contrast [10]. For this purpose, the tissue is illuminated by a short-pulsed laser and the absorbed photon energy leads to a rise in temperature. The resulting heat induces a thermoelastic expansion that generates a local pressure rise and emits acoustic waves, which are detected by a transducer [11,12]. Photoacoustic imaging combines the most compelling features of optical imaging and ultrasound, delivering both high optical contrast and high ultrasound resolution at depth in living organisms [13]. Hence, this technique offers great promise for the non-invasive exploration of biological tissues, leveraging differences in the optical absorption of underlying tissue components, such as hemoglobin, lipids, melanin, collagen and water. Moreover, endogenous photoacoustic signals from oxygenated hemoglobin (HbO_2) and deoxygenated hemoglobin (Hb)

* Corresponding author at: Department of Trauma and Reconstructive Surgery, Eberhard Karls University Tübingen, BG Trauma Center Tübingen, 72076 Tübingen, Germany.
E-mail address: maximilian.menger@uks.eu (M.M. Menger).

https://doi.org/10.1016/j.pacs.2022.100409
Received 23 January 2022; Received in revised form 14 August 2022; Accepted 25 September 2022
Available online 27 September 2022

reflect the microvasculature and provide structural and functional in vivo data on hemodynamics, neovascularization, tissue oxygenation and hypoxia [11,14].

Hence, there is a growing interest in the use of photoacoustic imaging for the investigation of the microcirculation in the fields of oncology, neurology, cardiovascular and metabolic diseases [15–17]. However, this imaging technique has not yet been implemented in the analysis of fracture repair and bone regeneration. Accordingly, we herein applied for the first time photoacoustic imaging for the investigation of non-unions and unions in a well-established murine fracture model.

2. Materials and methods

2.1. Animals

In this study, 37 male and female CD-1 mice with a mean body weight of 30–40 g and an age of 12–16 weeks were used. The animals were bred at the Institute for Clinical and Experimental Surgery, Saarland University, Germany, and housed at a regular light and dark cycle with free access to tap water and standard pellet food (Altromin, Lage, Germany).

All experiments were performed according to the German legislation on the protection of animals and the National Institutes of Health (NIH) Guide for the Care and Use of Laboratory Animals (Institute of Laboratory Animal Resources, National Research Council, Washington DC, USA). The experiments were approved by the local governmental animal protection committee (permit number: 13/2019).

2.2. Surgical procedure

Mice were anesthetized by intraperitoneal (i.p.) injection of ketamine (75 mg/kg body weight) and xylazine (15 mg/kg body weight). Under aseptic conditions, a ~4 mm medial parapatellar incision was performed at the right knee and the patella was dislocated laterally. After drilling a hole (diameter of 0.5 mm) into the intracondylar notch, a distally flattened pressfit 24 Gauge needle (diameter of 0.55 mm) was implanted intramedullary and the wound was closed. The pin was flattened at the distal end to avoid secondary dislocation. After insertion of the pin, the diaphysis of the femur was exposed by a lateral approach. Subsequently, a custom-made clip of 6 mm length was implanted as previously described ventrodorsally into the femur, laterally of the already implanted pin [18,19].

An osteotomy with a gap size of 0.25 mm was created with a Gigli saw in the union group. Care was taken to leave the periosteum intact. In the non-union group, a gap size of 1.8 mm was created by means of a spherical trephine under permanent saline solution cooling (Fig. 1a). Moreover, the periosteum was stripped 2 mm proximally and distally of the gap along the longitudinal axis of the femoral bone. The lateral incision was closed with interrupted sutures. The implant position was confirmed by radiography (Fig. 1b). All procedures were done under an operating microscope, guaranteeing a high level of precision. At 2 weeks (unions n = 5; non-unions n = 7), 5 weeks (unions n = 5; non-unions n = 5) and 10 weeks (unions n = 7; non-unions n = 8) the animals were sacrificed by an overdose of anesthetics and the femora were excised for further analyses.

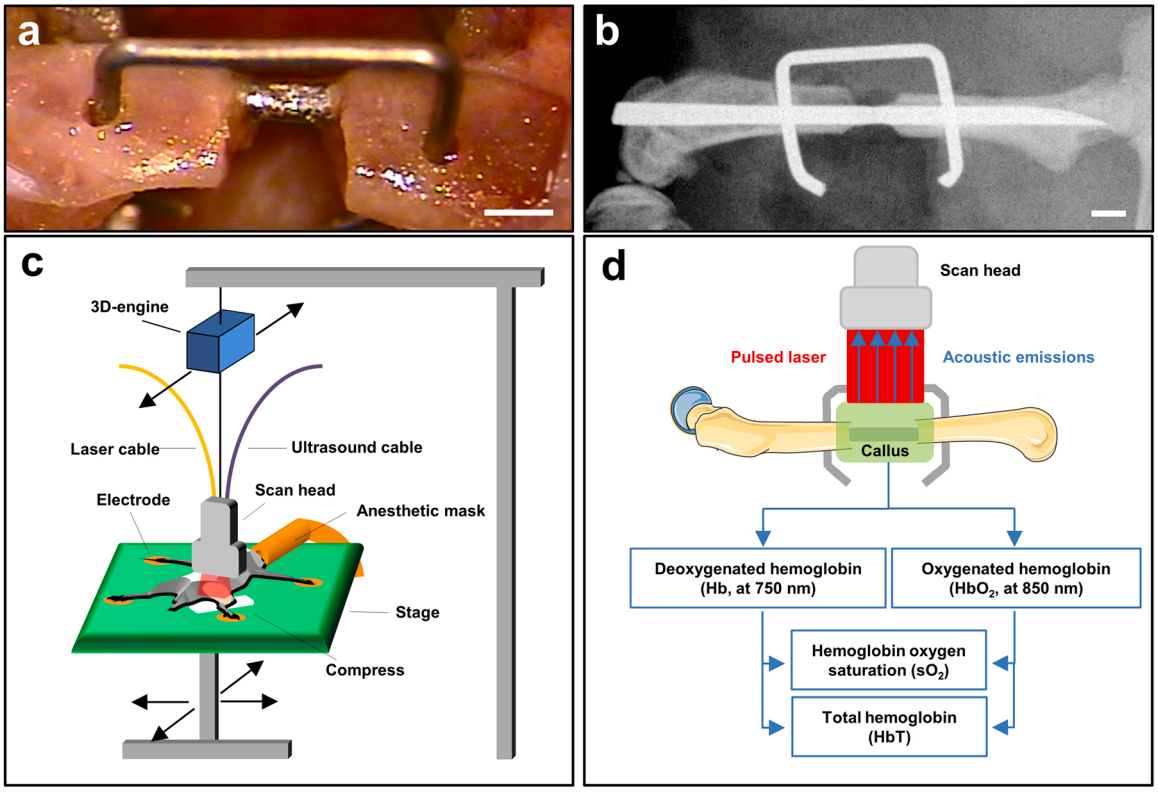

Fig. 1. Experimental setting of photoacoustic imaging. (a) Osteotomized mouse femur of the non-union group after stabilization with a costum-made clip. Scale bar: 1 mm. (b) Representative X-ray of a pin-clip osteosynthesis. Scale bar: 1 mm. (c) The animals were fixed in prone position on a heated stage and anesthetized with isoflurane through an anesthetic mask. Electrodes enabled the monitoring of vital parameters (heart rate and respiratory rate). A compress was positioned underneath the right hind limb to avoid artefact signals from the stage. The 3D-engine of the scan head enabled movement along the anterior-posterior axis. The movable observation stage allowed movement along the anterior-posterior and lateral axis. Thereby, a variety of recording settings could be adjusted to guarantee an optimal positioning for ultrasound and photoacoustic image acquisition. (d) A pulsed laser induced a thermoelastic expansion at the extinction wavelength of 750 nm for deoxygenated hemoglobin (Hb) and at 850 nm for oxygenated hemoglobin (HbO_2). The resulting acoustic emissions were detected by a transducer. OxyHemo-mode photoacoustic images were recorded at 750 nm and 850 nm to detect hemoglobin oxygen saturation (sO_2) and total hemoglobin (HbT).

2.3. X-ray

At 2, 5 and 10 weeks after surgery the animals were anesthetized again and ventrodorsal radiographs of the osteotomized femora were performed. Fracture healing was analyzed according to the classification of the Goldberg score with stage 0 indicating radiographic non-union, stage 1 indicating possible union and stage 2 indicating radiographic union [20].

2.4. Biomechanics

After removal of the soft tissue and implants, the bending stiffness of the osteotomized femora was measured by a 3-point-bending device using a non-destructive approach. This allowed for the subsequent use of the specimens for micro computed tomography (μCT) as well as histological and immunohistochemical investigations and, thus, to reduce the number of laboratory animals needed. Due to the different stages of healing, the loads, which had to be applied, markedly varied between the individual animals. Loading was stopped individually in every case when the actual load-displacement curve deviated more than 1% from linearity. Bending stiffness (N/mm) was calculated from the linear elastic part of the load-displacement diagram [21]. To account for differences in bone stiffness of the individual animals, the unfractured left femora were also analyzed, serving as an internal control. All values of the fractured femora are given in percent of the corresponding unfractured femora.

2.5. μCT

The specimens were scanned (Skysan 1172; Bruker, Billerica, MA, USA) at a spatial resolution of 6.5 μm with a standardized setup (tube voltage: 50 kV; current: 200 μA; intervals: 0.4°; exposure time: 3500 ms; filter: 0.5 mm aluminum). Images were stored in three-dimensional arrays. To express grey values as mineral content (bone mineral density (BMD)), calcium hydroxyapatite (CaHA) phantom rods with known BMD values (0.250 g and 0.750 g CaHA/cm^3) were employed for calibration. The region of interest (ROI) defining the novel bone was contoured manually excluding any original cortical bone. The thresholding allowed to distinguish soft tissue from bone tissue and the differentiation between lowly and highly mineralized bone (CTAnalyser; Bruker, Billerica, MA, USA). The thresholds to distinguish between lowly and highly mineralized bone were based upon visual inspection of the images, qualitative comparison with histological sections and other studies investigating bone repair and callus tissue by μCT [22–24]. A BMD with more than 0.642 g/cm^3 resulting in grey values of 98–255 was defined as highly mineralized bone. Lowly mineralized bone was assumed to have a BMD value between 0.410 g/cm^3 and 0.642 g/cm^3, resulting in grey values of 68–97. Tissue with grey values < 68 was defined as soft tissue.

The following parameters were calculated from the callus region of interest for each specimen: poorly mineralized bone volume, highly mineralized bone volume and bone volume fraction of tissue volume (BV/TV).

2.6. Ultrasound and photoacoustic imaging

High resolution ultrasound and photoacoustic imaging were performed at 2, 5 and 10 weeks after surgery by means of a Vevo LAZR system (FUJIFILM VisualSonics Inc.; Toronto, ON, Canada) equipped with a 256 element linear-array transducer (LZ 550, FUJIFILM VisualSonics Inc.) of 40 MHz center frequency. For this purpose, the animals were anesthetized with 1.5% isoflurane and subsequently fixed in prone position on a heated stage. The Vevo imaging station (FUJIFILM VisualSonics Inc.; Toronto, ON, Canada) with a mouse platform was used to constantly monitor the heart rate and respiratory rate and to maintain the body temperature at 36–37 °C. A gauze compress was positioned underneath the right hind limb to avoid artefact signals from the heated stage. The skin was shaved dorsally around the right thigh and sterile ultrasound gel was applied to avoid air interference with ultrasound coupling onto the animal (Fig. 1c).

For the three-dimensional ultrasound and the photoacoustic imaging, the scan head was linearly translated with a stepper motor over the entire femur and two-dimensional parallel images were acquired at regular spatial intervals of 50 μm (Fig. 1c). To obtain the oxygen saturation map (sO2), OxyHemo imaging mode from the Vevo LAZR is used, in which the acquisition system switches between the illumination wavelengths of 750 nm and 850 nm. The image acquisition and the oxygen saturation calculation was performed as described previously [25]. OxyHemo-mode photoacoustic images were recorded with a two-dimensional gain of 42 dB and the resulting acoustic emissions were detected by using the same ultrasound transducer (Fig. 1d). The reconstructed oxygen saturation images were illustrated as a multiparametric map in which red and blue pixels represent highly oxygenated regions and less oxygenated regions, respectively. To measure the total hemoglobin (HbT)/volume (1/mm^3) within the callus tissue, all detected signals at the two wavelengths were divided by the callus volume [26]. In addition, oxygen saturation (sO_2 average, %) within the callus tissue of unions and non-unions was evaluated, as described previously. Imaging parameters were kept constant between animals with the exception of TGC (time gain compensation) settings, which were adjusted to optimize the fluence variation at depth. All values were computed using the Vevo LAB 1.7.2. software (FUJIFILM VisualSonics Inc.).

2.7. Histology and histomorphometry

After biomechanical testing and μCT analyses, the bones were fixed in paraformaldehyde for 24 h. Subsequently, the specimens were embedded in a 30% sucrose solution for another 24 h and then frozen at − 80 °C. Longitudinal sections through the femoral axis with a thickness of 4 μm were cut by the Kawamotos film method for histomorphometric analyses and stained with Safranin-O. At a magnification of 12.5x (BX60 Microscope; Olympus, Shinjuku, Japan; Zeiss Axio Cam and Axio Vision 3.1, Zeiss) structural indices were calculated according to the recommendations of Gerstenfeld et al. [27]. The following histomorphometric parameters of the bone defects were evaluated: (i) total callus area; (ii) bone callus area; (iii) cartilaginous callus area and (iv) fibrous callus area. The total callus area was defined as all osseous, cartilaginous and fibrous callus tissue between the two drilling holes of the clip outside of the cortices. Pre-existing cortical bone of the proximal and distal fragment, however, was excluded. Each area was marked and calculated using the ImageJ analysis system (NIH, Bethesda, USA).

2.8. Immunohistochemistry

In order to analyze the cellular composition of non-unions, longitudinal sections with a thickness of 4 μm were cut. For the immunohistochemical detection of microvessels within the callus tissue, sections were stained with a monoclonal rat anti-mouse antibody against the endothelial cell marker CD31 (1:100; Abcam, Cambridge, UK). A goat anti-rat IgG-Alexa555 antibody served as secondary antibody (1:100; Life Technologies, Eugene, USA). Cell nuclei were stained with Hoechst 33342 (2 μg/mL; Sigma-Aldrich, Taufkirchen, Germany).

Additional sections were co-stained with a monoclonal rat anti-mouse antibody against CD31 (1:100; Abcam) and a rabbit anti-mouse antibody against α-smooth muscle actin (SMA) (Abcam) as primary antibodies. A goat anti-rat IgG Alexa555 antibody and a goat anti-rabbit Alexa488 antibody (1:100; Life Technologies) served as secondary antibodies. Cell nuclei were stained with Hoechst 33342.

On the sections, we assessed the density of CD31-positive microvessels and the fraction of CD31/α-SMA-positive microvessels. For this purpose seven high-power fields (HPF, 400x magnification) were

analyzed, one HPF was placed in a standardized manner in the central region of the callus, while three additional HPFs were placed on each site of the periosteal callus (Fig. 2).

2.9. Statistical analysis

All data are given as means ± SEM. After testing the data for normal distribution (Kolmogorov-Smirnov test) and equal variance (*F*-test), comparisons between the two groups were performed by the Student's *t*-test. For non-parametrical data, a Mann-Whitney *U*-test was used. To test for time effects within individual groups, groups were assessed by the one-way analysis of variance (One-way ANOVA). This was followed by the Student-Newman-Keuls post-hoc test. Linear correlation (Pearson's coefficient of correlation for parametric distribution or Spearman's coefficient of correlation for non-parametric distribution) was used to evaluate the correlation between the number of microvessels within the callus tissue and the measurements of sO_2 and HbT. All statistical analyses were performed using the SigmaPlot 13.0 software (Jandel Corporation, San Rafael, CA, USA). A p-value of < 0.05 was considered to indicate significant differences.

3. Results

3.1. X-ray

The radiographic analysis of unions revealed an increasing callus formation and bone bridging throughout the observation period of 10 weeks (Fig. 3a, c and e). In contrast, non-unions showed no signs of osseous bridging. X-rays revealed a reliable non-union formation with a large persisting gap between the bone fragments. Moreover, the shape of the adjoining bone fragments was rounded and narrowing towards the osteotomy gap, which is a typical sign of atrophic non-union formation (Fig. 3b, d and f). Accordingly, they exhibited a significantly decreased Goldberg score at 5 and 10 weeks after surgery when compared to unions (Table 1).

3.2. Biomechanics

The biomechanical analysis showed a significantly lower bending stiffness in non-unions at 2, 5 and 10 weeks after surgery when compared to unions (Fig. 3g). Of interest, a relative bending stiffness of 85% in relation to non-fractured femora in unions 10 weeks after surgery indicated a successful process of bone regeneration. On the other hand, a relative bending stiffness of $< 1\%$ in the non-union group confirmed the complete failure of fracture healing (Fig. 3g). Notably, the unfractured contralateral femora of both groups showed no significant differences in bending stiffness (data not shown).

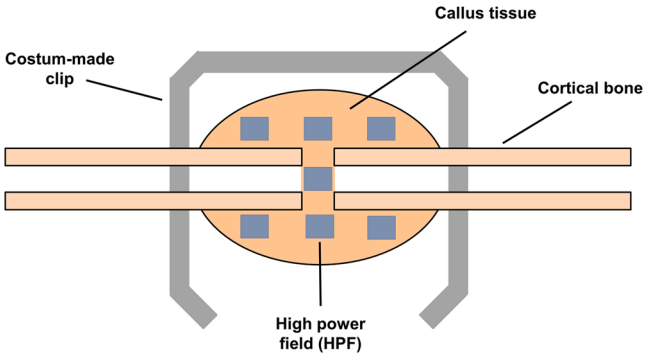

Fig. 2. Schematic illustration for the immunohistochemical analysis of microvessel distribution within the callus tissue of unions and non-unions. Blue rectangles represent the high power fields (HPFs, x400 magnification) for histological examination.

3.3. μCT

In line with the X-ray analysis, μCT images showed a typical pattern of secondary fracture healing in the union group with periosteal callus formation bridging the fracture gap at 5 weeks and bone remodeling at 10 weeks after surgery (Fig. 4a-c). In contrast, the non-union group exhibited no signs of adequate callus formation or osseous bridging throughout the observation period (Fig. 4d-f). The μCT analysis further revealed that the lowly and highly mineralized bone volume as well as the BV/TV did not differ at 2 weeks after surgery between the two study groups (Fig. 4g). However, we detected a significantly reduced lowly mineralized and highly mineralized bone volume as well as a lower BV/TV at 5 and 10 weeks after surgery in the non-union group (Fig. 4h, i and j).

3.4. Ultrasound and photoacoustic imaging

The ultrasound imaging enabled a clear and reliable visualization of the osteotomized femur. In the B-mode, the morphology of the various tissues and structures was clearly recognizable, including the bone, the osteotomy gap with associated callus tissue, the intramedullary pin and the muscle tissue surrounding the femur (Fig. 5a). A spectro-analysis made it possible to quantify the photoacoustic signal intensity of different tissues and structures across a wavelength range of 650–970 nm. Of interest, the tissues and structures showed different photoacoustic signal intensities at an extinction wavelength of 750 nm (hallmark for Hb) and 850 nm (hallmark for HbO_2) (Fig. 5b. c and d). The muscle tissue and also the intramedullary pin peaked in signal intensity towards the wavelength of 850 nm, whereas the callus tissue showed a more homogenous signal intensity across the wavelength spectrum (Fig. 5e). In contrast, the bone tissue peaked around a wavelength of 700 nm and decreased towards the wavelength of 850 nm (Fig. 5e). The monitored vital signs, i.e. heart rate, respiratory rate and body temperature, showed no significant difference between the two study groups, thus excluding any systemic influence on the measurement of photoacoustic parameters (Table 2).

Unions and non-unions were investigated at 2 (Fig. 6a-f, s, t), 5 (Fig. 6g-l, s, t) and 10 weeks (Fig. 6m-r, s, t) after surgery by ultrasound and photoacoustic imaging. For all investigations the ROI was placed in the fracture gap or in the osteotomy gap, respectively. In the B-mode (yellow dotted line) in the union group, the fracture can be nicely seen in Fig. 6a (2 weeks), while after 5 and 10 weeks indeed bony tissue within the ROI, i.e. former fracture gap, can be observed (Fig. 6 g and m), indicating bone healing. In the non-union group the osteotomy can also nicely been observed at 2 weeks within the yellow-dotted line in the ROI (Fig. 6d), while at 5 and 10 weeks no bony tissue is observed within the yellow-dotted ROI (Fig. 6j and p), indicating healing failure, i.e. non-union formation.

The ultrasound imaging showed the formation of callus tissue and osseous bridging at 5 and 10 weeks after surgery in the union group (Fig. 6g and m). In non-unions, however, the osteotomy gap was clearly visible throughout the entire observation period (Fig. 6d, j and p). Moreover, the photoacoustic analysis revealed a higher sO_2 within the callus tissue in unions at 2, 5 and 10 weeks after surgery when compared to non-unions (Fig. 6b, h and n vs. Fig. 6e, k and q and Fig. 6u). Of interest, at 5 and 10 weeks after surgery, the union group showed no significant decrease in sO_2 when compared to the early stage of fracture healing at 2 weeks after surgery (Fig. 6b, h, n and u). In contrast, non-unions revealed a significant decline in sO_2 from 2 weeks to 5 and 10 weeks after surgery (Fig. 6e, k, q and u).

The amount of HbT was also significantly enhanced in unions at 2 and 5 weeks after surgery when compared to non-unions (Fig. 6c and l vs. Fig. 6f and l and Fig. 6v). Notably, at 10 weeks after osteotomy the analysis showed no significant difference in the amount of HbT between the two study groups (Fig. 6o, r and v).

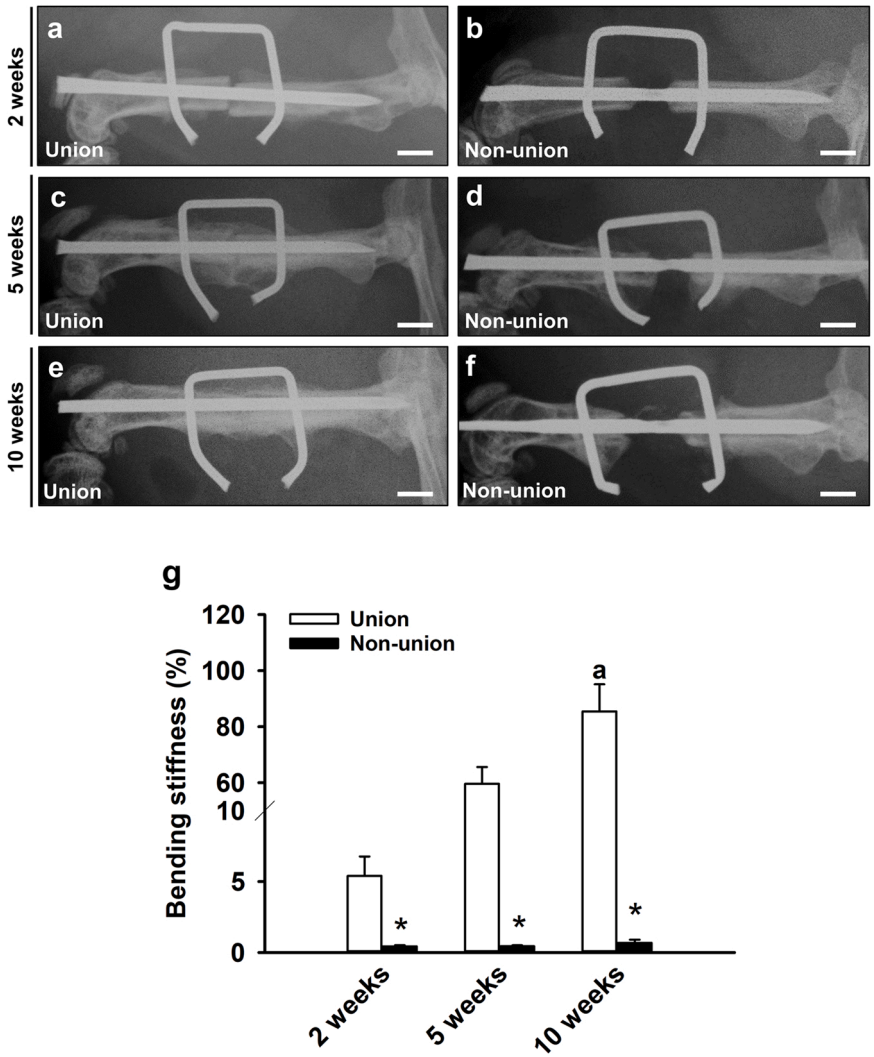

Fig. 3. X-ray and biomechanical analysis. (a-f) Representative X-rays of femora in unions (a, c, e) and non-unions (b, d, f) at 2 (a, b), 5 (c, d) and 10 weeks (e, f) after surgery. Scale bars: 2 mm. (g) Biomechanical analysis of bending stiffness of unions (white bars; n = 5–7) and non-unions (black bars; n = 5–8). Data are given in percent to the contralateral femora. Mean ± SEM; *p < 0.05 vs. union; a < 0.05 vs. 2 weeks.

Table 1
Radiographic analysis of unions (*white bars;* n = 5–8) and non-unions (*black bars;* n = 5–8) according to the Goldberg score at 2, 5 and 10 weeks after surgery.

	2 weeks	5 weeks	10 weeks
Goldberg score			
Union	0.4 ± 0.2	1.4 ± 0.2	2.0 ± 0.0[a]
Non-union	0.0 ± 0.0 *	0.0 ± 0.0 *	0.0 ± 0.0 *

Mean ± SEM; *p < 0.05 vs. union; a < 0.05 vs. 2 weeks.

3.5. Histomorphometry and immunohistochemistry

The histomorphometric analysis revealed a successful osseous bridging of the fracture gap with newly formed woven bone in the union group at 10 weeks after surgery (Fig. 7a). In the non-union group, however, there was a complete lack of osseous bridging with fibrous tissue remaining in the fracture gap at 10 weeks, indicating a reliable non-union formation (Fig. 7b). Moreover, the analysis of callus composition at 2, 5 and 10 weeks after surgery showed a significantly higher fraction of bone tissue in unions, whereas the amount of remnant fibrous tissue was significantly lower when compared to non-unions (Fig. 7c-e). Of note, the callus of unions showed a large amount of cartilage tissue at 2 weeks of fracture healing (Fig. 7c), which was found decreased at 5 and, particularly, at 10 weeks after surgery (Fig. 7d and e). In contrast, the callus of non-union showed an only slight amount of cartilage at 5 weeks (Fig. 7c, d and e).

In addition, the immunohistochemical analysis of the callus tissue showed a significant increase of microvessel density from 2 weeks to 5 weeks in both unions and non-unions (Fig. 7f, g, I, j and l). However, detailed analyses at both time points revealed a significantly higher density of CD31-positive microvessels in unions when compared to non-unions (Fig. 7f and g vs. Fig. 7i and j and Fig. 7l). After 10 weeks the analysis showed no significant differences between the two study groups (Fig. 7h, k and l).

The number of α-SMA-positive microvessels increased significantly within the callus tissue of unions at 5 and 10 weeks after surgery when compared to 2 weeks (Fig. 7m-o and s). In contrast, the callus tissue of non-unions revealed a slightly reduced number of microvessels with a perivascular α-SMA-positive cell layer at 2 weeks after surgery and a significantly reduced number of α-SMA-positive microvessels at 5 and 10 weeks after surgery (Fig. 7p-s). These findings indicate a lower maturation stage of the newly formed microvessels within the callus tissue of non-unions when compared to those of unions (Fig. 7s).

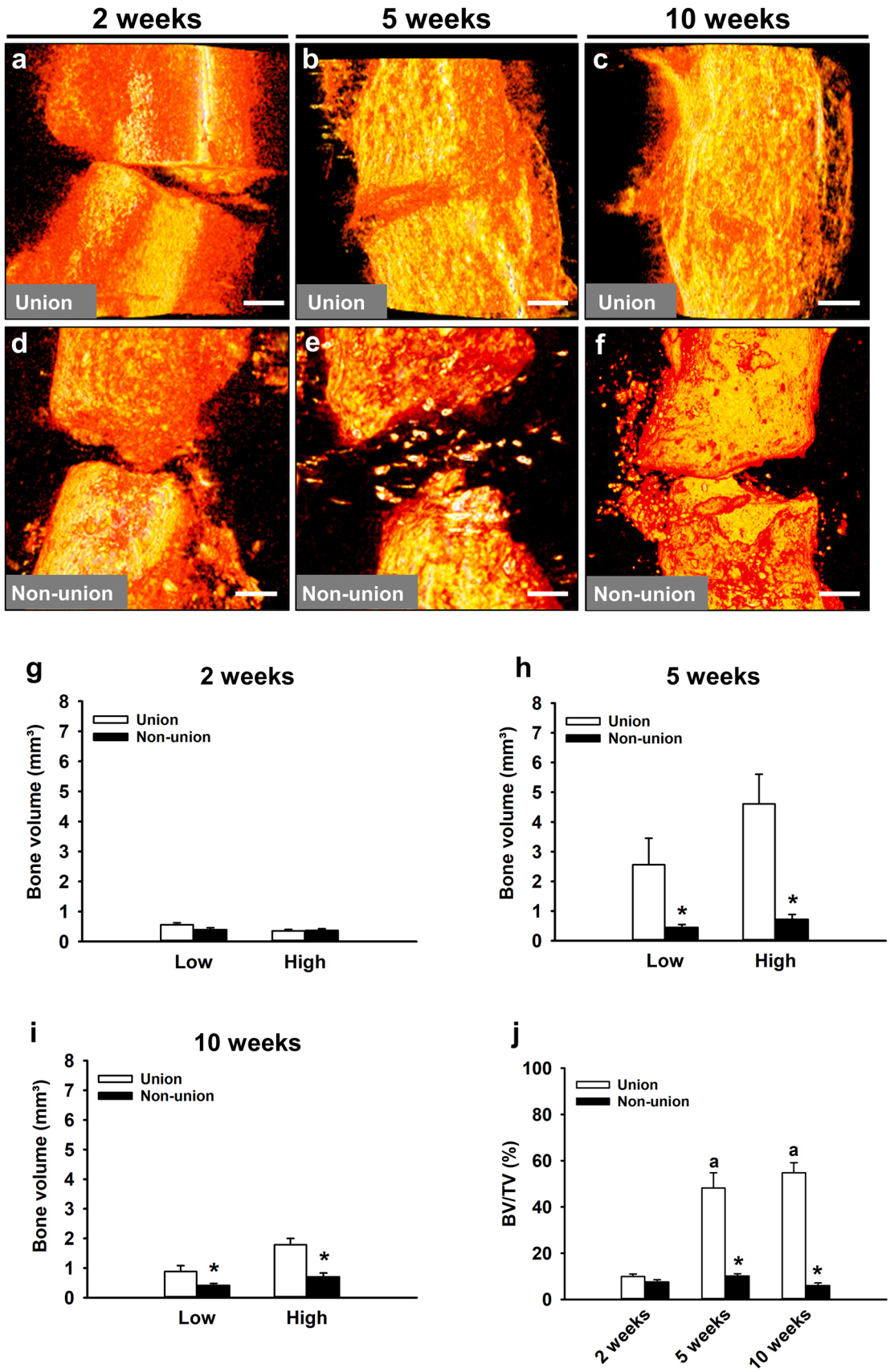

Fig. 4. μCT analysis. (a-f) Representative three-dimensional reconstructions of unions (a-c) and non-unions (d-f) at 2 (a, d), 5 (b, e) and 10 weeks (c, f) after surgery. Scale bars: 0.5 mm. (g-i) Analysis of lowly mineralized and highly mineralized bone volume (mm^3) in unions (white bars; n = 5–7) and non-unions (black bars; n = 5–8) at 2 (g), 5 (h) and 10 weeks (i) after surgery. (j) Analysis of the fraction of mineralized bone volume to tissue volume (BV/TV, %) in unions (white bars; n = 5–7) and non-unions (black bars; n = 5–8) at 2, 5 and 10 weeks after surgery. Mean ± SEM; *p < 0.05 vs. union; a < 0.05 vs. 2 weeks.

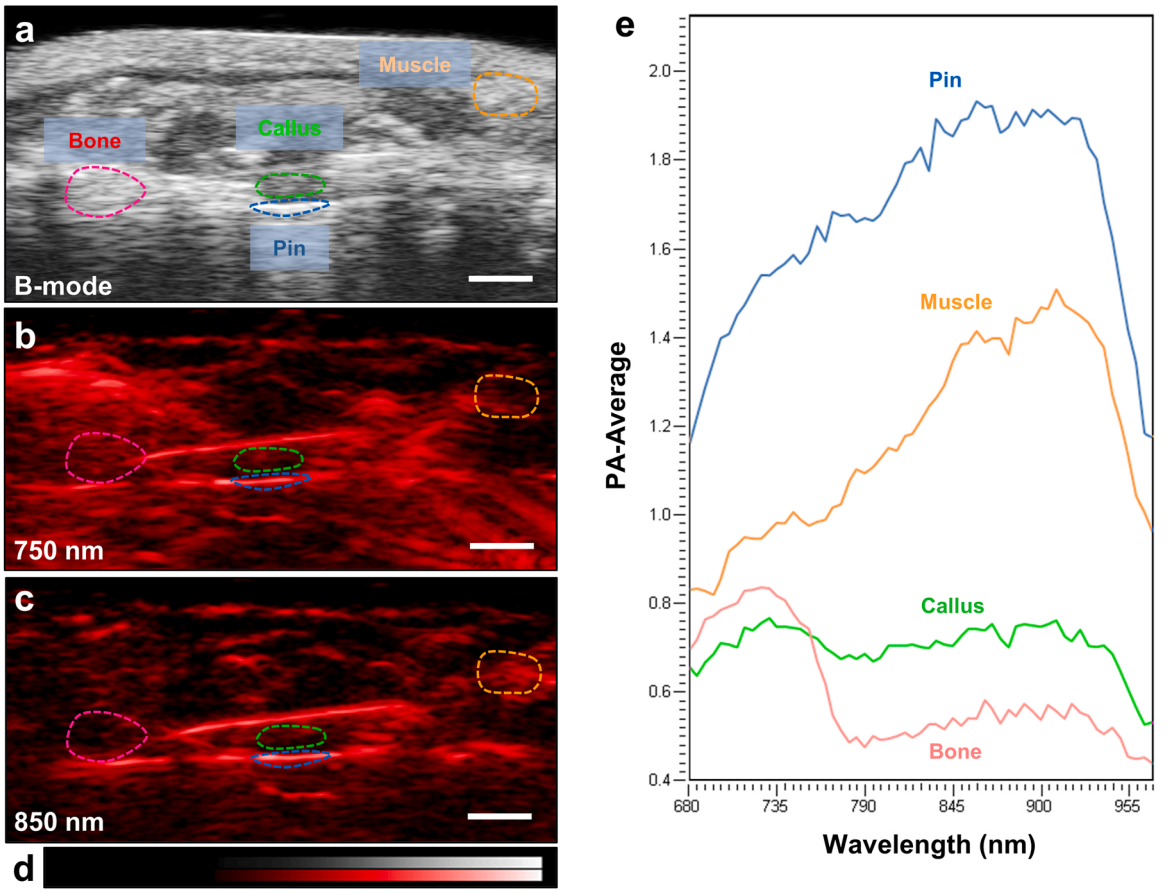

Fig. 5. Spectro-mode of photoacoustic imaging. (a) B-mode image of a non-union at 2 weeks after surgery. Ultrasound imaging allows the clear identification of structures and tissues, including bone, muscle, callus and implant (intramedullary pin). Scale bar: 2 mm. (b, c) Corresponding photoacoustic images of deoxygenated hemoglobin (Hb) at a wavelength of 750 nm (b) and oxygenated hemoglobin (HbO_2) at a wavelength of 850 nm (c). Scale bars: 2 mm. (d) Representative color bar of PA-Average. (e) Quantification of photoacoustic signals across the wavelength range of 680–970 nm of structures and tissues including bone, muscle, callus and implant (intramedullary pin).

Table 2
Vital signs (heart rate, respiratory rate and body temperature) of the animals in the union and non-union group during the photoacoustic imaging at 2, 5 and 10 weeks after surgery.

	2 weeks	5 weeks	10 weeks
HR (1/min)			
Union	453.5 ± 10.5	446.8 ± 59.3	444.7 ± 31.8
Non-union	472.1 ± 25.3	481.1 ± 42.5	494.0 ± 33.4
RR (1/min)			
Union	95.2 ± 8.2	113.1 ± 15.5	90.1 ± 14.3
Non-union	96.2 ± 8.2	126.6 ± 10.0	99.3 ± 5.4
T (C°)			
Union	37.1 ± 0.3	36.6 ± 0.4	36.6 ± 0.3
Non-union	36.5 ± 0.3	36.6 ± 0.4	36.1 ± 0.4

Mean ± SEM.
Heart rate (HR); respiratory rate (RR); body temperature (T)

3.6. Correlation between microvessel density and photoacoustic parameters

A linear correlation analysis was performed to determine the correlation between microvessel density and photoacoustic imaging parameters. Of interest, we found a positive correlation between the microvessel density and HbT values within the callus tissue of unions (Fig. 8a; r = 0.730) and an even higher positive correlation between these two parameters in non-unions (Fig. 8b; r = 0.896). Surprisingly, we found no significant correlation between the microvessel density and sO_2 within the callus tissue of unions and non-unions (Fig. 8c and d). In fact, we even found a slightly negative correlation between the microvessel density and sO_2 in the non-union group (Fig. 8d; r = - 0.272).

4. Discussion

Despite major efforts in experimental orthopedic research, the pathophysiology of vascularization in delayed healing and non-unions is still not fully understood. Accordingly, there is a lack of reliable methods to predict the risk of non-union formation for each individual patient and a lack of possibilities to intervene early with appropriate treatment strategies. To gain further insights in the deterioration of vascular development and temporal oxygenation patterns of non-union formation, we investigated for the first time unions and non-unions by a non-invasive photoacoustic imaging technique using an established murine fracture and non-union model. By this, we were able to determine the temporal course of photoacoustic imaging parameters in the callus of unions and non-unions and compared them to the microvessel density of the callus in corresponding histological specimens.

Photoacoustic imaging represents a state-of-the-art imaging technique that allows the investigation of vascular hemodynamics [28], microvascular networks [29,30], hemoglobin concentration and oxygen saturation [14,31] in a variety of tissues. In a recent study Chen et al. [32] applied photoacoustic microscopy in combination with the novel hypoxia-responsive probe HyP-650 in order to monitor intravascular oxygenation and tissue hypoxia in an experimental mouse model of hindlimb ischemia. Until now, however, there are only a few studies that

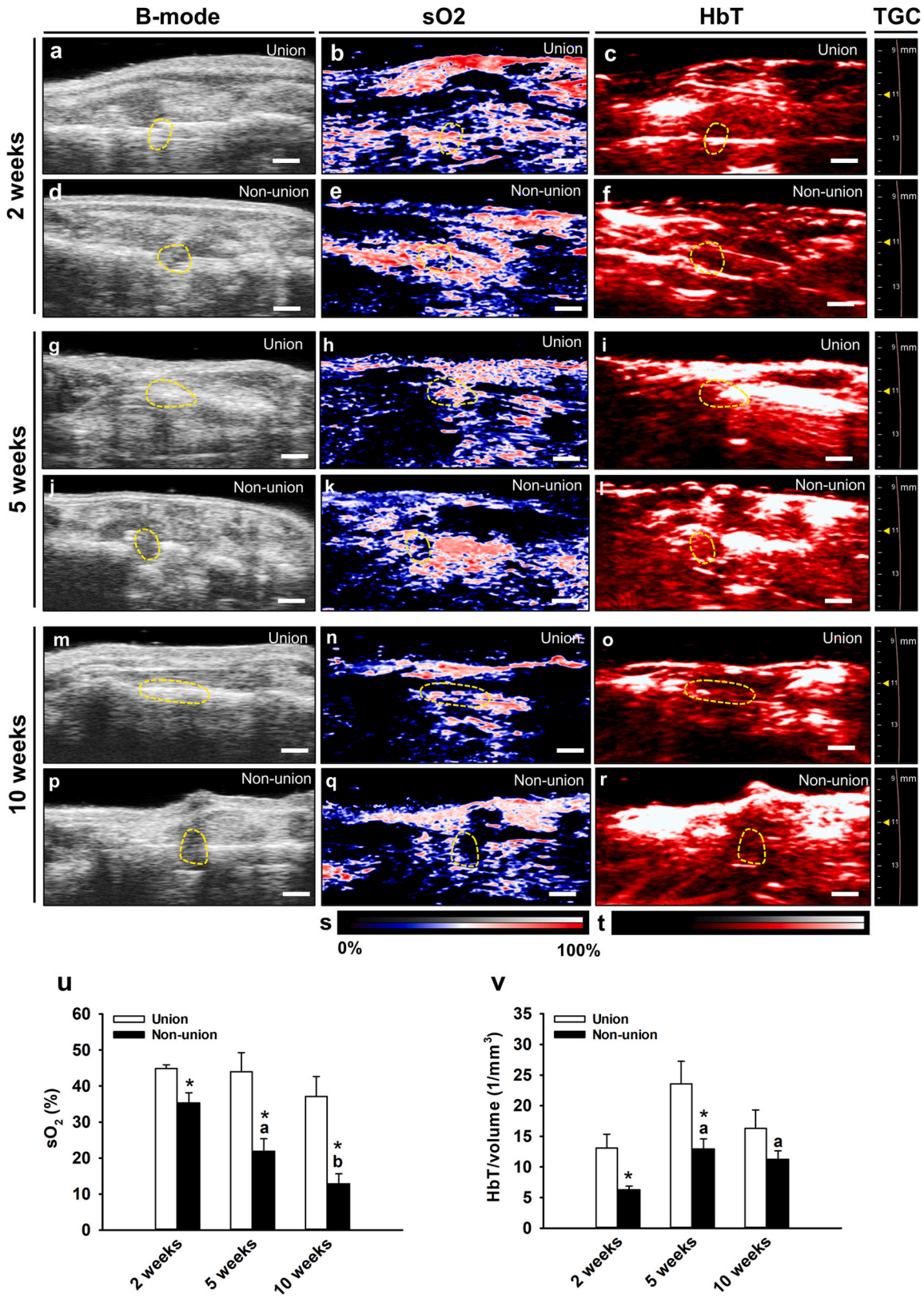

Fig. 6. Photoacoustic imaging analysis. (a-r) Representative images of B-mode, hemoglobin oxygen saturation (sO_2) and total hemoglobin (HbT) with corresponding time gain compensation (TGC) settings at 2, 5 and 10 weeks after surgery. The callus tissue (ROI) is marked with yellow broken lines. Scale bars: 2 mm. (s, t) Representative color bars of sO_2 (s) and HbT (t). (u) Analysis of sO_2 (%) in unions (white bars; n = 5–7) and non-unions (black bars; n = 5–8) at 2, 5 and 10 weeks after surgery. (v) Analysis of HbT/volume ($1/mm^3$) in unions (white bars; n = 5–7) and non-unions (black bars; n = 5–8) at 2, 5 and 10 weeks after surgery. Mean ± SEM; *p < 0.05 vs. union; a < 0.05 vs. 2 weeks; b < 0.05 vs. 2 and 5 weeks.

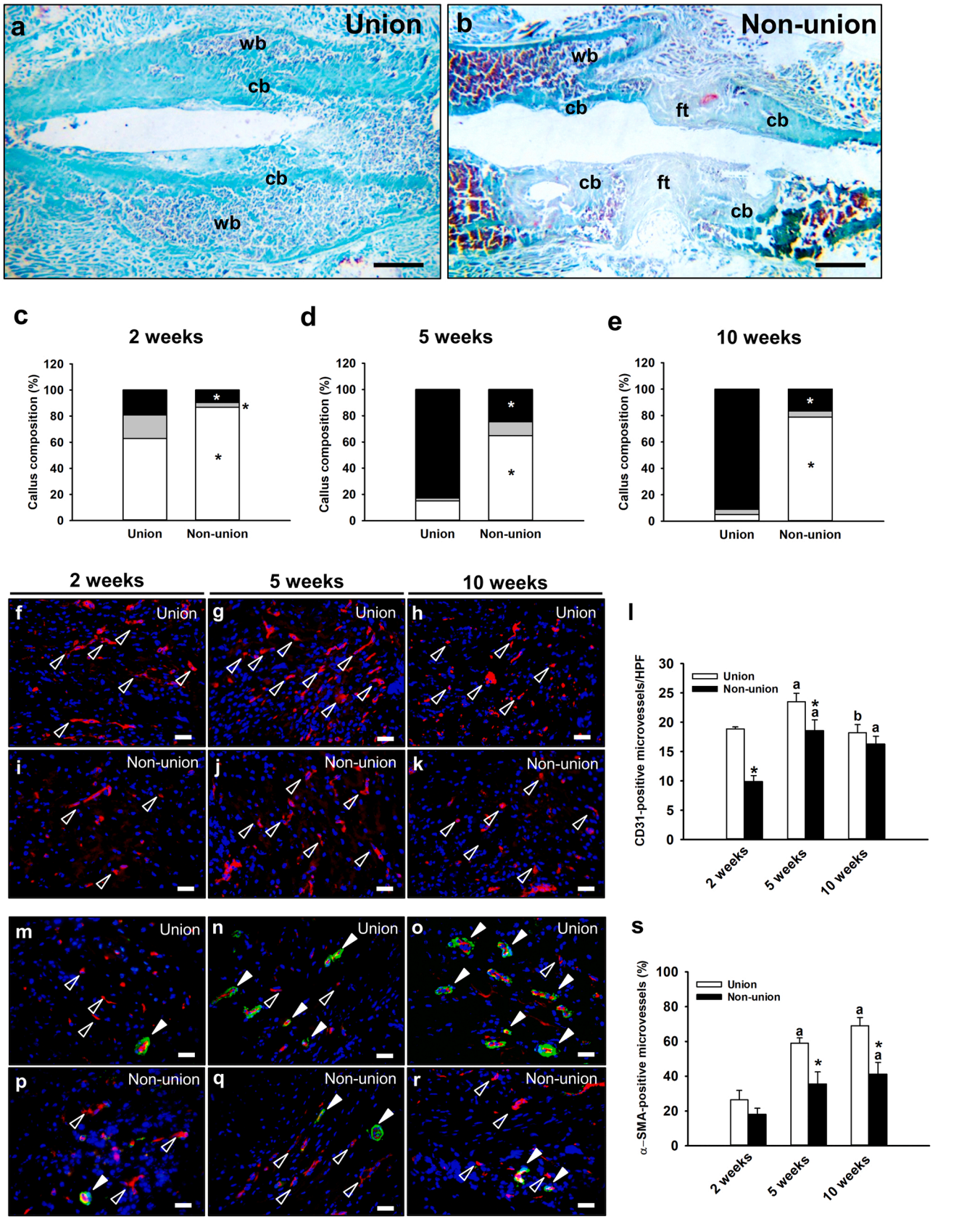

(caption on next page)

Fig. 7. Histomorphometric and immunohistochemical analysis. (a, b) Representative images of a Safranin-O-stained union (a) and non-union (b) at 10 weeks after surgery. Fibrous tissue (ft), woven bone (wb) and cortical bone (cb) are indicated. Scale bars: 1 mm. (c-e) Analysis of callus composition of unions (n = 5 – 7) and non-unions (n = 5–8) at 2 (c), 5 (d) and 10 weeks (e) after surgery. Callus composition including fibrous tissue (*white*), cartilaginous tissue (*grey*) and osseous tissue (*black*). (f-k) Representative immunohistochemical images of CD31-positive microvessels within the callus tissue of unions (f-h) and non-nions (i-k) at 2 (f and i), 5 (g and j) and 10 weeks (h and k) after surgery. Scale bars: 25 μm. (l) Analysis of CD31-positive microvessels within the callus tissue of unions (white bars; n = 5–7) and non-unions (black bars; n = 5–8) at 2, 5 and 10 weeks after surgery. (m-r) Representative immunohistochemical images of α-SMA-positive microvessels within the callus tissue of unions (m-o) and non-unions (p-r) at 2 (m and p), 5 (n and q) and 10 weeks after surgery (o and r). Scale bars: 25 μm. (s) Analysis of α-SMA-positive microvessels (%) within the callus tissue of unions (white bars; n = 5–7) and non-unions (black bars; n = 5–8) at 2 weeks, 5 weeks and 10 weeks after surgery. Mean ± SEM; *p < 0.05 vs. union; a < 0.05 vs. 2 weeks; b < 0.05 vs. 5 weeks.

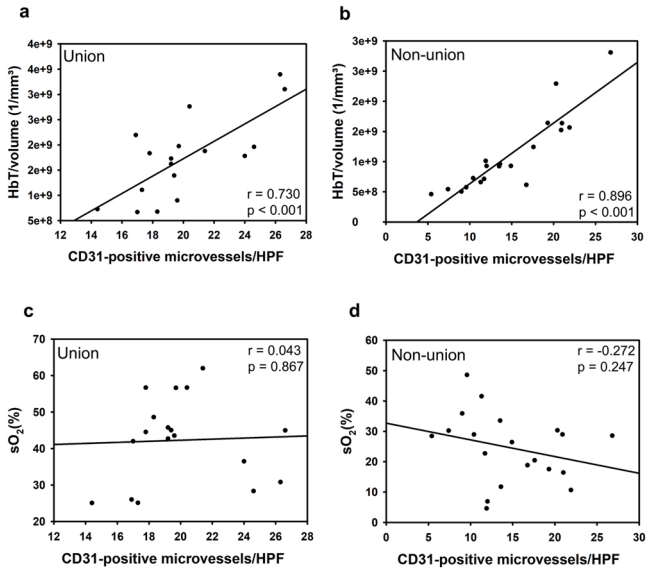

Fig. 8. Linear correlation analysis between microvessel density and photoacoustic imaging parameters. (a, b) Linear correlation analysis between microvessel density and HbT/volume within the callus tissue of unions (a) and non-unions (b). (c, d) Linear correlation analysis between microvessel density and sO_2 within the callus tissue of unions (c) and non-unions (d).

use photoacoustic imaging for applications in the field of orthopedic and bone research. Lui et al. [33] applied photoacoustic imaging in an experimental model of posttraumatic osteoarthritis for the non-invasive visualization of angiogenesis and hypoxia in synovial tissue. In addition, Estrada et al. [29] used a photoacoustic microscopy method in combination with ultrasound biomicroscopy for large-scale imaging of the calvarian microvasculature in living rodents. Moreover, photoacoustic imaging has been used for the diagnosis of Staphylococcus aureus-induced osteomyelitis in mice [34] and for the local assessment of intravascular oxygen saturation within the murine bone marrow cavity [35]. We herein now applied photoacoustic imaging for the first time to analyze vascularization and tissue oxygenation in fracture healing and non-union formation.

In the present study, we used a well-established pin-clip fracture model, which can mimic both successful fracture healing [19] as well as compromised bone regeneration, resulting in reliable non-union formation [18]. In the union group, we used a Gigli saw to create a small 0.25 mm defect in the femora of mice. The defect site showed clear signs of callus formation at 2 weeks and resulted in complete fracture healing at 5 and 10 weeks after surgery, as shown by biomechanical, radiological and histological analyses. In contrast, a large 1.8 mm defect was created by a spherical trephine with additional periosteal stripping in the non-union group. Accordingly, our analyses revealed the persistence of the fracture gap filled with abundant fibrous tissue and rounded adjoining bone fragments at 10 weeks after surgery, indicating atrophic non-union formation [36].

Unions and non-unions were analyzed by ultrasound and photoacoustic imaging, which allowed for the separate measurement of HbO_2, Hb, sO_2 and HbT [31]. Noteworthy, sO_2 can also be used as an indirect parameter to quantify tissue oxygenation and hypoxia [37]. In the present study, we found a significantly decreased sO_2 within the callus of non-unions when compared to unions. Moreover, sO_2 significantly declined over the time course of the healing process in the non-union group. Our histological analysis, on the other hand, revealed a similar density of CD31-positive microvessels within the callus tissue of unions and non-unions at 10 weeks after surgery. However, the detection of CD31-positive microvessels by immunohistochemistry is not necessarily associated with a functional vascular network, but may also represent forming and regressing vascular structures without the ability to sufficiently supply the surrounding tissue with oxygen. In line with this view, we detected a significantly reduced number of microvessels exhibiting a perivascular α-SMA-positive cell layer, suggesting a lower maturation stage of the newly developed microvascular network within the callus tissue of non-unions when compared to unions [38,39]. These findings indicate that the functionality of the microvascular network in non-unions gradually deteriorates, ultimately leading to an avital and biologically inert environment. The callus tissue in unions showed a stable sO_2 during the observation period, which appears to be a crucial prerequisite for successful bone regeneration. This sufficient supply with oxygen in the union group may be explained by an enhanced number of microvessels and an increased ratio of α-SMA-positive vessels within the callus tissue when compared to non-unions, indicating a mature and fully functional microvascular system.

The HbT concentration and microvessel density showed a similar temporal course throughout the observation period in the union and non-union group. In fact, our analyses revealed a good positive correlation between the HbT concentration and CD31-positive microvessels within the callus tissue of unions and non-unions, making HbT a promising photoacoustic parameter for the non-invasive assessment of vascularization in bone regeneration and orthopedic research. However, vascularization does not necessarily correspond to microvascular perfusion.

Interestingly, our data showed no significant correlation between the sO_2 and microvessel density in non-unions and unions. In non-unions this may be explained by the fact that the number of newly formed microvessels is not an indicator for the functionality of the microvascular network. A high vascular density may be associated with a low or even ceased microvascular perfusion and, thus, a low sO_2 within the callus tissue. The low tissue oxygenation may even promote further angiogenesis, resulting in further vascularization without perfusion, which may represent a type of "frustrated angiogenesis". Accordingly, several other experimental studies detected a considerable vessel density in non-unions with no sign of bone healing progression [40–42].

In unions, the microvasculature is subject to an extensive remodeling and reorganization that occurs during the formation of soft callus tissue containing fibroblasts and chondroblasts and its subsequent transformation in newly formed woven bone tissue. During this process, the vessel density within the callus tissue strongly differs temporarily and spatially between the different types of tissue [43]. Therefore, the sole number of microvessels may be an insufficient and oversimplified parameter for the correlation with sO_2 within the callus tissue also during successful bone regeneration.

Photoacoustic imaging represents a powerful novel diagnostic technology to investigate microvascular functionality in bone regeneration.

Potential applications in preclinical orthopedic research include the monitoring of oxygen saturation within the callus tissue during the treatment with pro-osteogenic pharmacological compounds [44], innovative bone scaffold materials and sophisticated cell-based tissue engineering constructs [45]. In addition, photoacoustic imaging may be used in clinical practice in addition to conventional X-ray and CT diagnostics as a feasible screening tool for the early detection of delayed healing and non-union formation. A possible clinical study could monitor the oxygen saturation and total hemoglobin within the callus tissue from an early healing time point onwards. Subsequently the non-invasive photoacoustic imaging could deliver decisive data to determine at an early stage of bone healing, which fractures are at a high risk of resulting in non-union formation. In addition, the resulting data can be used to help decide on a possible revision surgery, thus facilitating the decision-making process for the treating surgeon. In addition, photoacoustic imaging displays a non-invasive method to evaluate osteoinductive treatment methods, such as extracorporeal shock wave therapy (ESWT) [46] or systemic treatment with teriparatide [47]. Moreover, photoacoustic imaging may provide vital information on the oxygen saturation within the bone tissue during revision surgery and may help to decide on the callus area, which tissue should be excised before definite osteosynthesis.

In summary, we herein studied for the first time the callus tissue of unions and non-unions in mice by photoacoustic imaging. Our data reveal that HbT positively correlates with the immunohistochemically assessed microvessel density within the callus tissue, making it a versatile tool for the analysis of vascularization in orthopedic research. Our data further show that the oxygen saturation in non-unions significantly declines throughout the 10-weeks observation period, most likely due to an altered microvascular perfusion despite an existing microvasculature. In the future, photoacoustic imaging will be helpful to evaluate preclinical treatment strategies, such as biophysical applications, systemic pharmacological interventions and sophisticated tissue engineering approaches. In addition, this novel imaging technology may be used in clinical practice as non-invasive screening tool for the monitoring of bone healing progress and non-union formation.

Declaration of Competing Interest

The authors declare that they have no known competing financial interests or personal relationships that could have appeared to influence the work reported in this paper.

Data availability

Data will be made available on request.

Acknowledgments

We are grateful for the excellent technical assistance of Sandra Hans and Caroline Bickelmann (Institute for Clinical & Experimental Surgery, Saarland University, Germany). The authors thank Servier Medical Art for providing access to designed medical elements (https://smart.servier.com/), supporting the generation of graphical items in this publication.

References

[1] T.A. Einhorn, L.C. Gerstenfeld, Fracture healing: mechanisms and interventions, Nat. Rev. Rheuma 11 (2015) 45–54. ⟨http://www.ncbi.nlm.nih.gov/pubmed/25266456⟩.

[2] P. Garcia, T. Histing, J.H. Holstein, M. Klein, M.W. Laschke, R. Matthys, A. Ignatius, B. Wildemann, J. Lienau, A. Peters, B. Willie, G. Duda, L. Claes, T. Pohlemann, M.D. Menger, Rodent animal models of delayed bone healing and non-union formation: a comprehensive review, Eur. Cell Mater. 26 (2013) 1–12, discussion 12-4, ⟨https://www.ncbi.nlm.nih.gov/pubmed/23857280⟩.

[3] M.M. Menger, M.W. Laschke, M. Orth, T. Pohlemann, M.D. Menger, T. Histing, Vascularization strategies in the prevention of non-union formation, Tissue Eng. Part B Rev. (2020). ⟨https://www.ncbi.nlm.nih.gov/pubmed/32635857⟩.

[4] J.M. Kanczler, R.O. Oreffo, Osteogenesis and angiogenesis: the potential for engineering bone, Eur. Cell Mater. 15 (2008) 100–114. ⟨http://www.ncbi.nlm.nih.gov/pubmed/18454418⟩.

[5] D. Paley, M.A. Catagni, F. Argnani, A. Villa, G.B. Benedetti, R. Cattaneo, Ilizarov treatment of tibial nonunions with bone loss, Clin. Orthop. Relat. Res (1989) 146–165. ⟨http://www.ncbi.nlm.nih.gov/pubmed/2924458⟩.

[6] B.G. Weber, C. Brunner, The treatment of nonunions without electrical stimulation, Clin. Orthop. Relat. Res (1981) 24–32. ⟨http://www.ncbi.nlm.nih.gov/pubmed/7030568⟩.

[7] C.T. Hu, S.C. Offley, Z. Yaseen, R.J. O'Keefe, C.A. Humphrey, Murine model of oligotrophic tibial nonunion, J. Orthop. Trauma 25 (2011) 500–505. ⟨http://www.ncbi.nlm.nih.gov/pubmed/21738067⟩.

[8] S. Santavirta, Y.T. Konttinen, D. Nordstrom, A. Makela, T. Sorsa, M. Hukkanen, P. Rokkanen, Immunologic studies of nonunited fractures, Acta Orthop. Scand. 63 (1992) 579–586. ⟨http://www.ncbi.nlm.nih.gov/pubmed/1471500⟩.

[9] H.C. Brownlow, A. Reed, A.H. Simpson, The vascularity of atrophic non-unions, Injury 33 (2002) 145–150. ⟨http://www.ncbi.nlm.nih.gov/pubmed/11890916⟩.

[10] R.A. Kruger, Photoacoustic ultrasound, Med Phys. 21 (1994) 127–131. ⟨https://www.ncbi.nlm.nih.gov/pubmed/8164577⟩.

[11] M. Li, Y. Tang, J. Yao, Photoacoustic tomography of blood oxygenation: A mini review, Photoacoustics 10 (2018) 65–73. ⟨https://www.ncbi.nlm.nih.gov/pubmed/29988848⟩.

[12] R.A. Kruger, P. Liu, Y.R. Fang, C.R. Appledorn, Photoacoustic ultrasound (PAUS)–reconstruction tomography, Med Phys. 22 (1995) 1605–1609. ⟨https://www.ncbi.nlm.nih.gov/pubmed/8551984⟩.

[13] X. Wang, Y. Pang, G. Ku, X. Xie, G. Stoica, L.V. Wang, Noninvasive laser-induced photoacoustic tomography for structural and functional in vivo imaging of the brain, Nat. Biotechnol. 21 (2003) 803–806. ⟨https://www.ncbi.nlm.nih.gov/pubmed/12808463⟩.

[14] X. Wang, X. Xie, G. Ku, L.V. Wang, G. Stoica, Noninvasive imaging of hemoglobin concentration and oxygenation in the rat brain using high-resolution photoacoustic tomography, J. Biomed. Opt. 11 (2006), 024015. ⟨https://www.ncbi.nlm.nih.gov/pubmed/16674205⟩.

[15] B. Shrestha, F. DeLuna, M.A. Anastasio, J. Yong Ye, E.M. Brey, Photoacoustic Imaging in Tissue Engineering and Regenerative Medicine, Tissue Eng. Part B Rev. 26 (2020) 79–102. ⟨https://www.ncbi.nlm.nih.gov/pubmed/31854242⟩.

[16] R. Chen, S. Huang, T. Lin, H. Ma, W. Shan, F. Duan, J. Lv, J. Zhang, L. Ren, L. Nie, Photoacoustic molecular imaging-escorted adipose photodynamic-browning synergy for fighting obesity with virus-like complexes, Nat. Nanotechnol. 16 (2021) 455–465. ⟨https://www.ncbi.nlm.nih.gov/pubmed/33526836⟩.

[17] J. Lv, Y. Xu, L. Xu, L. Nie, Quantitative functional evaluation of liver fibrosis in mice with dynamic contrast-enhanced photoacoustic imaging, Radiology 300 (2021) 89–97. ⟨https://www.ncbi.nlm.nih.gov/pubmed/33904773⟩.

[18] P. Garcia, J.H. Holstein, S. Maier, H. Schaumloffel, F. Al-Marrawi, M. Hannig, T. Pohlemann, M.D. Menger, Development of a reliable non-union model in mice, J. Surg. Res 147 (2008) 84–91. ⟨http://www.ncbi.nlm.nih.gov/pubmed/18061614⟩.

[19] P. Garcia, J.H. Holstein, T. Histing, M. Burkhardt, U. Culemann, A. Pizanis, R. J. Wirbel, T. Pohlemann, M.D. Menger, A new technique for internal fixation of femoral fractures in mice: impact of stability on fracture healing, J. Biomech. 41 (2008) 1689–1696. ⟨https://www.ncbi.nlm.nih.gov/pubmed/18462739⟩.

[20] V.M. Goldberg, A. Powell, J.W. Shaffer, J. Zika, G.D. Bos, K.G. Heiple, Bone grafting: role of histocompatibility in transplantation, J. Orthop. Res 3 (1985) 389–404. ⟨http://www.ncbi.nlm.nih.gov/pubmed/3906062⟩.

[21] T. Histing, J.H. Holstein, P. Garcia, R. Matthys, A. Kristen, L. Claes, M.D. Menger, T. Pohlemann, Ex vivo analysis of rotational stiffness of different osteosynthesis techniques in mouse femur fracture, J. Orthop. Res 27 (2009) 1152–1156. ⟨http://www.ncbi.nlm.nih.gov/pubmed/19215028⟩.

[22] P. Bosemark, H. Isaksson, M.M. McDonald, D.G. Little, M. Tagil, Augmentation of autologous bone graft by a combination of bone morphogenic protein and bisphosphonate increased both callus volume and strength, Acta Orthop. 84 (2013) 106–111. ⟨http://www.ncbi.nlm.nih.gov/pubmed/23409846⟩.

[23] E.F. Morgan, Z.D. Mason, K.B. Chien, A.J. Pfeiffer, G.L. Barnes, T.A. Einhorn, L. C. Gerstenfeld, Micro-computed tomography assessment of fracture healing: relationships among callus structure, composition, and mechanical function, Bone 44 (2009) 335–344. ⟨http://www.ncbi.nlm.nih.gov/pubmed/19013264⟩.

[24] H. Isaksson, I. Grongroft, W. Wilson, C.C. van Donkelaar, B. van Rietbergen, A. Tami, R. Huiskes, K. Ito, Remodeling of fracture callus in mice is consistent with mechanical loading and bone remodeling theory, J. Orthop. Res 27 (2009) 664–672. ⟨http://www.ncbi.nlm.nih.gov/pubmed/18985689⟩.

[25] A. Needles, A. Heinmiller, J. Sun, C. Theodoropoulos, D. Bates, D. Hirson, M. Yin, F.S. Foster, Development and initial application of a fully integrated photoacoustic micro-ultrasound system, IEEE Trans. Ultrason Ferroelectr. Freq. Control 60 (2013) 888–897. ⟨https://www.ncbi.nlm.nih.gov/pubmed/23661123⟩.

[26] F.S. Frueh, B. Jelvani, C. Scheuer, C. Korbel, B.S. Kim, P. Giovanoli, N. Lindenblatt, Y. Harder, E. Ampofo, M.D. Menger, M.W. Laschke, Short-term molecular and cellular effects of ischemia/reperfusion on vascularized lymph node flaps in rats, PLoS One 15 (2020), e0239517. ⟨https://www.ncbi.nlm.nih.gov/pubmed/33021999⟩.

[27] L.C. Gerstenfeld, T.J. Wronski, J.O. Hollinger, T.A. Einhorn, Application of histomorphometric methods to the study of bone repair, J. Bone Min. Res 20 (2005) 1715–1722. ⟨http://www.ncbi.nlm.nih.gov/pubmed/16160729⟩.

[28] L.J. Rich, M. Seshadri, Photoacoustic imaging of vascular hemodynamics: validation with blood oxygenation level-dependent MR imaging, Radiology 275 (2015) 110–118. ⟨https://www.ncbi.nlm.nih.gov/pubmed/25423146⟩.
[29] H. Estrada, J. Rebling, U. Hofmann, D. Razansky, Discerning calvarian microvascular networks by combined optoacoustic ultrasound microscopy, Photoacoustics 19 (2020), 100178. ⟨https://www.ncbi.nlm.nih.gov/pubmed/32215252⟩.
[30] O. Ogunlade, J.O.Y. Ho, T.L. Kalber, R.E. Hynds, E. Zhang, S.M. Janes, M. A. Birchall, C.R. Butler, P. Beard, Monitoring neovascularization and integration of decellularized human scaffolds using photoacoustic imaging, Photoacoustics 13 (2019) 76–84. ⟨https://www.ncbi.nlm.nih.gov/pubmed/30805295⟩.
[31] S. Mallidi, K. Watanabe, D. Timerman, D. Schoenfeld, T. Hasan, Prediction of tumor recurrence and therapy monitoring using ultrasound-guided photoacoustic imaging, Theranostics 5 (2015) 289–301. ⟨https://www.ncbi.nlm.nih.gov/pubmed/25553116⟩.
[32] M. Chen, H.J. Knox, Y. Tang, W. Liu, L. Nie, J. Chan, J. Yao, Simultaneous photoacoustic imaging of intravascular and tissue oxygenation, Opt. Lett. 44 (2019) 3773–3776. ⟨https://www.ncbi.nlm.nih.gov/pubmed/31368965⟩.
[33] Z. Liu, M. Au, X. Wang, P.B. Chan, P. Lai, L. Sun, Y. Zheng, L. Rong, C. Wen, Photoacoustic imaging of synovial tissue hypoxia in experimental post-traumatic osteoarthritis, Prog. Biophys. Mol. Biol. 148 (2019) 12–20. ⟨https://www.ncbi.nlm.nih.gov/pubmed/29601835⟩.
[34] X. Lu, R. Chen, J. Lv, W. Xu, H. Chen, Z. Ma, S. Huang, S. Li, H. Liu, J. Hu, L. Nie, High-resolution bimodal imaging and potent antibiotic/photodynamic synergistic therapy for osteomyelitis with a bacterial inflammation-specific versatile agent, Acta Biomater. 99 (2019) 363–372. ⟨https://www.ncbi.nlm.nih.gov/pubmed/31465882⟩.
[35] C. Wood, K. Harutyunyan, D.R.T. Sampaio, M. Konopleva, R. Bouchard, Photoacoustic-based oxygen saturation assessment of murine femoral bone marrow in a preclinical model of leukemia, Photoacoustics 14 (2019) 31–36. ⟨https://www.ncbi.nlm.nih.gov/pubmed/31049286⟩.
[36] M. Orth, A.K. Shenar, C. Scheuer, B.J. Braun, S.C. Herath, J.H. Holstein, T. Histing, X. Yu, W.L. Murphy, T. Pohlemann, M.W. Laschke, M.D. Menger, VEGF-loaded mineral-coated microparticles improve bone repair and are associated with increased expression of epo and RUNX-2 in murine non-unions, J. Orthop. Res 37 (2019) 821–831. ⟨http://www.ncbi.nlm.nih.gov/pubmed/30835895⟩.
[37] M. Gerling, Y. Zhao, S. Nania, K.J. Norberg, C.S. Verbeke, B. Englert, R.V. Kuiper, A. Bergstrom, M. Hassan, A. Neesse, J.M. Lohr, R.L. Heuchel, Real-time assessment of tissue hypoxia in vivo with combined photoacoustics and high-frequency ultrasound, Theranostics 4 (2014) 604–613. ⟨https://www.ncbi.nlm.nih.gov/pubmed/24723982⟩.
[38] T. Spater, M.M. Menger, R.M. Nickels, M.D. Menger, M.W. Laschke, Macrophages promote network formation and maturation of transplanted adipose tissue-derived microvascular fragments, J. Tissue Eng. 11 (2020), 2041731420911816, ⟨https://www.ncbi.nlm.nih.gov/pubmed/32313616⟩.
[39] J. Rudzitis-Auth, R.M. Nickels, M.D. Menger, M.W. Laschke, Inhibition of cyclooxygenase-2 suppresses the recruitment of endothelial progenitor cells in the microvasculature of endometriotic lesions, Am. J. Pathol. 188 (2018) 450–460. ⟨https://www.ncbi.nlm.nih.gov/pubmed/29154961⟩.
[40] A.A. Reed, C.J. Joyner, H.C. Brownlow, A.H. Simpson, Human atrophic fracture non-unions are not avascular, J. Orthop. Res 20 (2002) 593–599. ⟨http://www.ncbi.nlm.nih.gov/pubmed/12038636⟩.
[41] A.A. Reed, C.J. Joyner, S. Isefuku, H.C. Brownlow, A.H. Simpson, Vascularity in a new model of atrophic nonunion, J. Bone Jt. Surg. Br. 85 (2003) 604–610. ⟨http://www.ncbi.nlm.nih.gov/pubmed/12793572⟩.
[42] P. Garcia, A. Pieruschka, M. Klein, A. Tami, T. Histing, J.H. Holstein, C. Scheuer, T. Pohlemann, M.D. Menger, Temporal and spatial vascularization patterns of unions and nonunions: role of vascular endothelial growth factor and bone morphogenetic proteins, J. Bone Jt. Surg. Am. 94 (2012) 49–58. ⟨http://www.ncbi.nlm.nih.gov/pubmed/22218382⟩.
[43] K.K. Sivaraj, R.H. Adams, Blood vessel formation and function in bone, Development 143 (2016) 2706–2715. ⟨https://www.ncbi.nlm.nih.gov/pubmed/27486231⟩.
[44] J.H. Holstein, M. Orth, C. Scheuer, A. Tami, S.C. Becker, P. Garcia, T. Histing, P. Morsdorf, M. Klein, T. Pohlemann, M.D. Menger, Erythropoietin stimulates bone formation, cell proliferation, and angiogenesis in a femoral segmental defect model in mice, Bone 49 (2011) 1037–1045. ⟨http://www.ncbi.nlm.nih.gov/pubmed/21851867⟩.
[45] Y.S. Zhang, L.V. Wang, Y. Xia, Seeing through the surface: non-invasive characterization of biomaterial-tissue interactions using photoacoustic microscopy, Ann. Biomed. Eng. 44 (2016) 649–666. ⟨https://www.ncbi.nlm.nih.gov/pubmed/26471785⟩.
[46] A. Cacchio, L. Giordano, O. Colafarina, J.D. Rompe, E. Tavernese, F. Ioppolo, S. Flamini, G. Spacca, V. Santilli, Extracorporeal shock-wave therapy compared with surgery for hypertrophic long-bone nonunions, J. Bone Jt. Surg. Am. 91 (2009) 2589–2597. ⟨http://www.ncbi.nlm.nih.gov/pubmed/19884432⟩.
[47] N.H. Moon, J.H. Jang, W.C. Shin, S.J. Jung, Effects of teriparatide on treatment outcomes in osteoporotic hip and pelvic bone fractures: meta-analysis and systematic review of randomized controlled trials, Hip Pelvis 32 (2020) 182–191. ⟨https://www.ncbi.nlm.nih.gov/pubmed/33335866⟩.

Maximilian Menger received his medical degree from the University of Cologne. Subsequently, he started working as a resident in the department of Trauma- and Reconstructive Surgery at the Saarland university hospital in Homburg/Saar. During this time, he started his experimental research focusing on the pathophysiology of non-union formation and bone healing in the aged. He is now working as a resident in the Department of Trauma- and Reconstructive Surgery/BG Klinik Tübingen at the Eberhard Karls University Tübingen and is continuing his clinical work as well as experimental research activities.

Tina Histing started her medical career and research activity at the Saarland university hospital in Homburg/Saar. She has establish a variety of preclinical models to study fracture healing in mice. In 2020 she was appointed as clinical director and head physician of the Department of Trauma- and Reconstructive Surgery/BG Klinik Tübingen at the Eberhard Karls University Tübingen. Tina Histing is currently supervising a variety of preclinical and clinical projects focusing on bone healing in the aged and non-union formation.